Tidal flow separation at protruding beach nourishments

Radermacher, Max; de Schipper, Matthieu; Swinkels, Cilia M.; MacMahan, Jamie; Reniers, Ad

DOI
10.1002/2016JC011942

Publication date
2016

Document Version
Final published version

Published in
Journal Of Geophysical Research-Oceans

AGU PUBLICATIONS

JGR

Journal of Geophysical Research: Oceans

RESEARCH ARTICLE

10.1002/2016JC011942

Tidal flow separation at protruding beach nourishments

Max Radermacher [1,2], Matthieu A. de Schipper [1,3], Cilia Swinkels[4], Jamie H. MacMahan [5], and Ad J.H.M. Reniers[1,6]

[1]Faculty of Civil Engineering and Geosciences, Department of Hydraulic Engineering, Delft University of Technology, Delft, Netherlands, [2]WaveDroid, Delft, Netherlands, [3]Shore Monitoring and Research, The Hague, Netherlands, [4]Harbour, Coastal and Offshore Engineering, Deltares, Delft, Netherlands, [5]Department of Oceanography, Naval Postgraduate School, Monterrey, California, USA, [6]Applied Morphodynamics, Deltares, Delft, Netherlands

Key Points:
- Tidal flow separation and eddy formation can occur at protruding beach nourishments
- The intensity of tidal eddies varies with the spring-neap cycle
- Eddy characteristics around shallow coastline perturbations can be predicted from depth-averaged numerical model results

Correspondence to:
M. Radermacher,
m.radermacher@tudelft.nl

Citation:
Radermacher, M., M. A. de Schipper, C. Swinkels, J. H. MacMahan, and A. J. H. M. Reniers (2017), Tidal flow separation at protruding beach nourishments, *J. Geophys. Res. Oceans*, *122*, doi:10.1002/2016JC011942.

Received 9 MAY 2016
Accepted 28 NOV 2016
Accepted article online 20 DEC 2016

Abstract In recent years, the application of large-scale beach nourishments has been discussed, with the Sand Motor in the Netherlands as the first real-world example. Such protruding beach nourishments have an impact on tidal currents, potentially leading to tidal flow separation and the generation of tidal eddies of length scales larger than the nourishment itself. The present study examines the characteristics of the tidal flow field around protruding beach nourishments under varying nourishment geometry and tidal conditions, based on extensive field observations and numerical flow simulations. Observations of the flow field around the Sand Motor, obtained with a ship-mounted current profiler and a set of fixed current profilers, show that a tidal eddy develops along the northern edge of the mega-nourishment every flood period. The eddy is generated around peak tidal flow and gradually gains size and strength, growing much larger than the cross-shore dimension of the coastline perturbation. Based on a 3 week measurement period, it is shown that the intensity of the eddy modulates with the spring-neap tidal cycle. Depth-averaged tidal currents around coastline perturbations are simulated and compared to the field observations. The occurrence and behavior of tidal eddies is derived for a large set of simulations with varying nourishment size and shape. Results show that several different types of behavior exist, characterized by different combinations of the nourishment aspect ratio, the size of the nourishment relative to the tidal excursion length, and the influence of bed friction.

1. Introduction

Beach nourishments have been applied world-wide as an effective method of mitigating coastal erosion problems for several decades already [*Hamm et al*., 2002]. In recent years, large-scale multifunctional beach nourishments have been advocated based on morphological, ecological, recreational, and economic arguments [*Stive et al*., 2013; *De Vriend et al*., 2015]. Large beach nourishments protrude from the coastline and therefore cause strong interactions between the nourishment and the surrounding coastal hydrodynamics. Notably, the character of the tidal flow field around such large nourishments might change drastically, see Figure 1. Separation of shore-parallel periodic tidal flow at a perturbation and the associated formation of tidal eddies can have consequences for the morphological development of the coast [*Pingree*, 1978; *Ferentinos and Collins*, 1980] and the nourishment. Furthermore, if the nourishment represents a significant recreational value, concerns regarding the impact of tidal flow separation on swimmer safety might arise [*Van den Hoek et al*., 2014]. Finally, enhanced tidal mixing and spatially varying bed shear stresses can affect the mixing of nutrients [*Signell and Geyer*, 1990] and the quality of the benthic habitat [*Nowell and Jumars*, 1984]. Adequate field observations and numerical parameter sensitivity studies of tidal flow perturbation by beach nourishments are currently lacking, which hampers prediction of the tidal flow field and related morphological, ecological and recreational impacts around nourishment sites.

This study is aimed at examining the characteristics of the tidal flow field around protruding beach nourishments under varying nourishment geometry and tidal conditions. First, the behavior of the tidal flow field is assessed in a real-world situation based on a set of field observations, which were obtained near a particularly large beach nourishment in the Netherlands (sections 2 and 3). Multiple measurement techniques are combined to support interpretation of the spatiotemporally varying tidal flow field. Then, a numerical model is presented and compared to the field data (section 4). Subsequently, this model is employed to perform a

Figure 1. The Sand Motor mega-nourishment in the Netherlands (left) just after construction in 2011, with turbidity patterns at the sea surface revealing signs of a separating tidal flow field, and (right) in 2014, after approximately 3 years of morphological development. Images by Joop van Houdt/Rijkswaterstaat.

parameter sensitivity study, examining the behavior of the tidal flow field (occurrence of flow separation and eddy formation) as a function of tidal flow characteristics and the geometry of the perturbation (section 5).

Studies of the impact of beach nourishments on tidal flow are rare. This is mainly due to the fact that traditional beach nourishments generally have a cross-shore extent in the order of 100 m, and therefore do not significantly obstruct alongshore tidal currents. The best analogy of tidal flow around a very large nourishment is found in studies of tidal flow around headlands. *Pingree* [1978] obtained field observations of tidal flow around a headland in the English Channel, showing that large eddies exist off the headland as a result of flow separation. Similar findings were reported based on observations with fixed current meters around headlands in the Bristol Channel [*Ferentinos and Collins*, 1980].

Geyer and Signell [1990] mapped tidal currents around Gay Head (MA, USA) and found large-scale eddies, which were formed as a result of tidal flow separation. These eddies are not shed from the coastline, as can be observed in flow past an obstruction in stationary flow, but remain in the near vicinity of the headland. Just after their formation around peak tidal flow the eddies are small, but they gradually grow in size to reach their maximum around slack tide. Subsequently, the eddy rapidly disappears as the tidal flow reverses. Spiraling secondary flow perpendicular to the main flow direction was found off the headland tip, forced by strong centrifugal accelerations [*Geyer*, 1993]. An elaborate parameter sensitivity study was conducted by *Signell and Geyer* [1991], using a numerical model of the tidal flow around Gay Head. They identified four different flow regimes, depending on a combination of friction, the tidal excursion length, and the headland geometry. The situation at Gay Head, with a tidal eddy remaining attached to the shoreline, was found to occur in case of high friction and a relatively large headland compared to the tidal excursion length. From the spreading of artificial, passive tracers in the same numerical model, *Signell and Geyer* [1990] concluded that flow separation around headlands can significantly enhance the dispersion of floating, suspended, or dissolved matter.

Following similar observations around islands by *Wolanski et al*. [1984], tidal flow separation in island wakes was studied by various researchers. *Black and Gay* [1987] highlighted the role of the local streamwise pressure gradient in island wakes. Flow separation is the result of an adverse streamwise pressure gradient in wall-bounded flow [e.g., *Simpson*, 1989]. Often the adverse pressure gradient is caused by decelerating flow downstream of an obstacle (e.g., a headland). However, as regions with strong tidal flows typically also experience significant tidal water level gradients, adverse pressure gradients, and associated flow separation can also result from the vertical tide. *Black and Gay* [1987] found that in many cases, tidal eddies near an obstacle are driven by a combination of both mechanisms. They form initially due to decelerating flow downstream of the obstacle and subsequently grow larger under the influence of adverse large-scale tidal water level gradients. This is reflected by the behavior of the growing tidal eddies around Gay Head [*Signell and Geyer*, 1991]. A similar influence of flow instationarity was shown to exist in laminar, oscillatory pipe flow along a wall disturbance [*Sobey*, 1983; *Ralph*, 1986], where an initial, separating eddy may interact with

vorticity generated around flow reversal. *Hench and Luettich* [2003] addressed the competition between various forcing mechanisms of tidal flow separation very illustratively by evaluating the terms of the streamwise and transverse momentum balance around Beaufort Inlet (NC, USA). They underlined the streamwise balance between the pressure gradient and advective acceleration during the early ebb and flood phases and between the pressure gradient and local acceleration during the late ebb and flood phases.

Instationary tidal flow around these different perturbations can be described based on the dimensionless Keulegan-Carpenter number K_C (equation (1)) and the dimensionless disturbance aspect ratio α (equation (2)),

$$K_C = \frac{U_p T}{L_a} \tag{1}$$

$$\alpha = \frac{L_c}{L_a} \tag{2}$$

where U_p represents the offshore peak tidal flow velocity, T is the tidal period, L_a is the alongshore disturbance length scale (the disturbance being a headland, nourishment, island, etc.), and L_c is the cross-shore disturbance length scale. L_a is measured parallel to the overall coastline orientation between the disturbance tip and the point where it connects to the surrounding coastline. The value of K_C can be regarded as the relative importance of advective acceleration compared to local acceleration, or alternatively as the tidal excursion length over the streamwise disturbance length. A small value of K_C indicates a large disturbance size compared to the tidal excursion. Likewise, if K_C is large, the disturbance size is small compared to the tidal excursion. The interpretation of α is straightforward, with a larger value indicating a more pronounced disturbance shape and a smaller value indicating a less pronounced disturbance shape.

Beach nourishments are typically situated along sandy shelf coasts. The water depth in these environments is relatively shallow. *Wolanski et al*. [1984] and *Tomczak* [1988] suggested that the importance of bottom friction can be expressed through a shallow water Reynolds number Re_z (equation (3)), which was found to correlate well with different types of island wake behavior observed by *Wolanski et al*. [1984] and *Pattiaratchi et al*. [1986].

$$Re_z = \frac{U_p H^2}{K_z L_c} \tag{3}$$

In equation (3), H denotes the water depth and K_z is the vertical diffusion coefficient, which is calculated here with the formulation suggested by *Wolanski et al*. [1984]. Essentially, Re_z expresses the relative importance of advection compared to bottom friction. This study will expand existing studies by focusing particularly on the role of disturbance size and shape, which may vary strongly between different nourishments. Characteristics of the separating tidal flow field (eddy size, strength, and lifetime) will be quantified under a large, realistic range of conditions (expressed by the value ranges of K_C and α), thereby placing earlier qualitative findings in a broader perspective. Large variations in Re_z are not taken into account, because the cross-shore beach profile around beach nourishments is generally mild and the influence of bottom friction is relatively high (values of Re_z considered in this study are O(1)). Instationarity of the tidal flow is shown to be more important than variable bed friction under these circumstances.

2. Field Setup

Field observations for this study were obtained around the Sand Motor [*Stive et al*., 2013], a mega-scale beach nourishment situated at the Dutch coastline south of The Hague in the Delfland coastal cell. The Sand Motor was constructed in 2011 as a 17.5 Mm^3 hook-shaped peninsula. It is expected to nourish the adjacent coastline throughout the coming decades, relying on natural sediment transport processes to spread the sand.

The Delfland coastal cell is a 20 km stretch of North Sea coastline, located in between the Rotterdam and The Hague harbor breakwaters at the southern and northern end, respectively (Figure 2). The Sand Motor mega-nourishment was originally constructed between 6 and 8 km south of The Hague, but has meanwhile extended its signature through alongshore sediment transport (Figure 1). Its approximate aspect ratio in

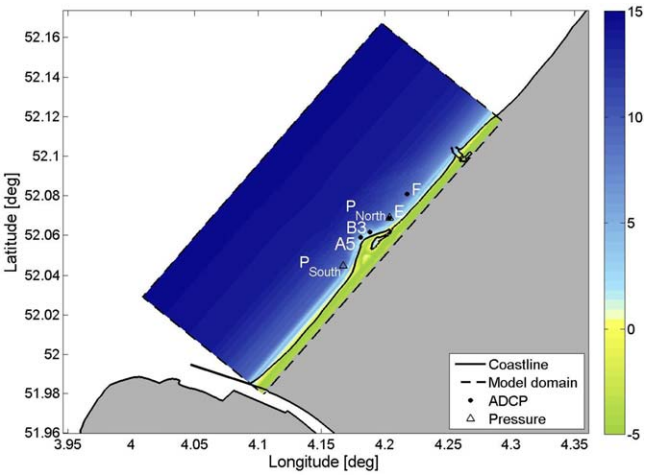

Figure 2. Overview of the Delfland coastal cell, the instrument setup, and the numerical model domain (dashed lines). Shading inside the model domain marks the model bathymetry. The solid line indicates the real-world position of the coastline as a reference. The harbor moles of Rotterdam and The Hague, which are visible in the real-world coastline, have been omitted in the model.

September 2014 was $\alpha \sim 0.3$. The foreshore is shallow, with the 15 m depth contour located 5 km offshore. The Delfland coast is a microtidal environment, the tidal range varying between 1.8 and 1.4 m over one spring-neap cycle [*Wijnberg*, 2002]. The tide at the southern North Sea is a counterclockwise rotating Kelvin wave, which drives tidal currents in alongshore direction (flood current directed to the north-east along the Delfland coast). Depth-averaged peak tidal currents are in the order of 0.7 m/s and the phase difference between the surface elevation and tidal currents is close to 0°.

Just south of the Rotterdam harbor breakwater, the main outflow of the Rhine river is located (Figure 2). This outflow is associated with a considerable freshwater runoff of on average 2200 m^3/s. The resulting, tidally pulsating freshwater plume regularly approaches the shoreline near the Sand Motor and constitutes a region of freshwater influence (ROFI), which stretches northward along the entire Dutch coast [*Souza and Simpson*, 1997]. The presence of freshwater induces temporally varying vertical and horizontal density gradients [*De Boer et al.*, 2006].

In order to determine the characteristics of the tidal flow field around the northern half of the Sand Motor, a set of field measurements was obtained in September and October 2014 during the large, multidisciplinary Mega-Perturbation Experiment (MegaPEX). Part of the instrument setup is presented in Figure 2.

An alongshore array of four upward looking acoustic doppler current profilers (ADCP's) was deployed stretching from the tip (i.e., most seaward point) of the Sand Motor to a location 3.5 km farther north-east. The ADCP profile measurements provided continuous time series of flow velocity. Stations A5 and B3 were located at 4 m depth, station E at 6 m and station F at 9 m. Table 1 lists the properties of all four current profilers. Fifteen minutes averaged flow velocities were linearly interpolated to mid-depth values, based on the instantaneous water level and local water depth, to obtain a proxy for the depth-averaged flow velocity. Actual depth averaging over the ADCP bins was considered inappropriate, as the shallow ADCP moorings did not always cover a representative part of the water column to justify depth averaging. A comparison was made between mid-depth velocities and depth-averaged velocities at stations E and F, which had a relatively large coverage of the water column compared to A5 and B3. The correlation coefficient between both parameters for the full deployment period equals 0.99 (significant to the 95% confidence level) at both stations for alongshore velocities with an RMSE of 2 cm/s at E and 3 cm/s at F, while the correlation coefficient for cross-shore velocities is 0.95 at E and 0.68 at F (both significant to the 95% confidence level), with an RMSE of 2 and 3 cm/s, respectively. As this study primarily focuses on alongshore velocity components, the use of mid-depth velocities is considered appropriate.

Pressure transducers were located north and south of the Sand Motor (P_{north} and P_{south}) at 6 and 9 m depth, respectively, see Figure 2. The 15 min averaged pressure data were used to determine tidal water levels throughout the measurement period.

Table 1. ADCP Characteristics

Station	Water Depth (m)	Bottom Bin Center (m)	Bin Height (m)	Averaging Time
A5	4	−3.2	0.5	1 s
B3	4	−2.6	0.5	1 s
E	6	−4.1	0.5	5 min
F	9	−6.2	0.5	5 min
Ship	n/a	n/a	0.25	2 s

Next to the fixed instruments, a 13 h ship-mounted ADCP campaign was conducted on 27 September. Every hour a set of transects was surveyed by the ship. The measurement domain gradually shifted northward as the tidal current turned from ebb to

flood. This resulted in (tidal) flow measurements at a high spatial resolution, covering one full tidal cycle. Properties of the downward-facing 600 kHz ADCP are given in Table 1. The position and orientation of the ship was measured with a real-time kinematic differential GPS (RTK-DGPS) and a gyroscope-corrected compass. Observed flow velocities were corrected for the navigation speed of the ship by making use of the ADCP's bottom tracking functionality. Along the ship's navigation tracks, data were interpolated to discrete grid points. The velocity at a grid point was determined from ADCP profiles obtained within 100 m from that point, using interpolation weights based on the reciprocal distance to the grid point. Finally, velocities were averaged over all vertical bins to obtain the depth-averaged velocity.

These in situ observations were complemented with data from an X-band radar station, which was situated on top of a dune just north of the Sand Motor. Time-averaged backscatter intensity images [e.g., *Dankert et al*., 2003; *Haller et al*., 2014] have supported a qualitative understanding of flow patterns around the Sand Motor. A sequence of these images can be found in *Radermacher et al*. [2015], but further analysis of the radar data is omitted here.

3. Field Observations

First, the ship-mounted ADCP data are presented. Due to its high spatial resolution, this data set provides a synoptic overview of the tidal flow pattern. Subsequently the fixed ADCP data set, which is sparse in space but has a higher temporal resolution and coverage, provides flow characteristics over the course of multiple tidal cycles.

The ship-mounted ADCP data were collected on 27 September 2014. On this day, the tidal range was relatively large (1.6 m, spring tide), wave energy was low (0.5 m significant wave height), and winds were weak (2.5 m/s wind velocity at 10 m above sea level). This implies a dominant role of the tidal forcing of the flow compared to other forcing mechanisms (waves and wind). The data are therefore suitable to study the tidal flow field around the Sand Motor.

Six consecutive flow fields that were measured with the ship-mounted ADCP during the flood phase of the tide are shown in Figure 3. Every plot shows measurements obtained within half an hour from the given timestamp. At 16:30 h, the observed depth-averaged flow vectors show the initiation of tidal flow separation and reversal of the flow direction along the leeward edge of the nourishment. From that moment onward, a tidal eddy starts to develop. The eddy grows in alongshore and cross-shore extent, eventually extending well beyond the most seaward point of the Sand Motor (19:30 h) and enhancing further contraction of the main flood flow. Toward slack tide, the flow velocity in the eddy decreases, while the eddy still grows in size (20:30 h) and ceases to exist (21:30 h). Measurements obtained during the ebb phase do not extend far enough in southern direction to properly cover the flow field downstream of the mega-nourishment and are therefore not shown.

The temporal behavior of the flow is examined in more detail with time series of 15 min averaged surface elevation, alongshore pressure gradient and alongshore flow velocities at mid-depth from all four fixed ADCP stations on 27 September 2014 (Figure 4). During early flood, alongshore flow velocities at the four locations rise similarly, until approximately 16:30 h. The peak flood velocity at station A5 is 0.25 to 0.35 m/s higher than the peak flood velocity at the other three stations. The fall of alongshore flow velocity at stations B3 and E sets in earlier than at the other two stations and turns negative 1.5 (E) to 2.5 (B3) h before flow reversal at A5 and F. This coincides with flow separation and eddy formation (Figure 3), with B3 and E being temporarily situated in the return flow of the eddy. It takes about 2 h before the eddy has gained enough size (approximate diameter larger than 1 km) to cover stations B3 and E (Figure 3). At station F, the peak flood velocity is lower than at station A5. This difference can be attributed to accelerated tidal flow at A5 due to flow contraction. In addition, the tidal flow requires a certain distance downstream of the eddy to recover from flow separation. Within this lee zone, peak flow velocities are relatively low.

The local maximum in the alongshore flow velocity signals around 19:30 h at stations A5 and B3 cannot be explained by the tidal forcing alone. Most probably, these local peaks are related to the passage of the freshwater plume of the river Rhine. From analysis of time-averaged X-band radar imagery, it was confirmed that the front of the plume reaches the tip of the Sand Motor at that time. Furthermore, similar velocity peaks occur regularly at all four stations, including station F, which is located well outside the region of

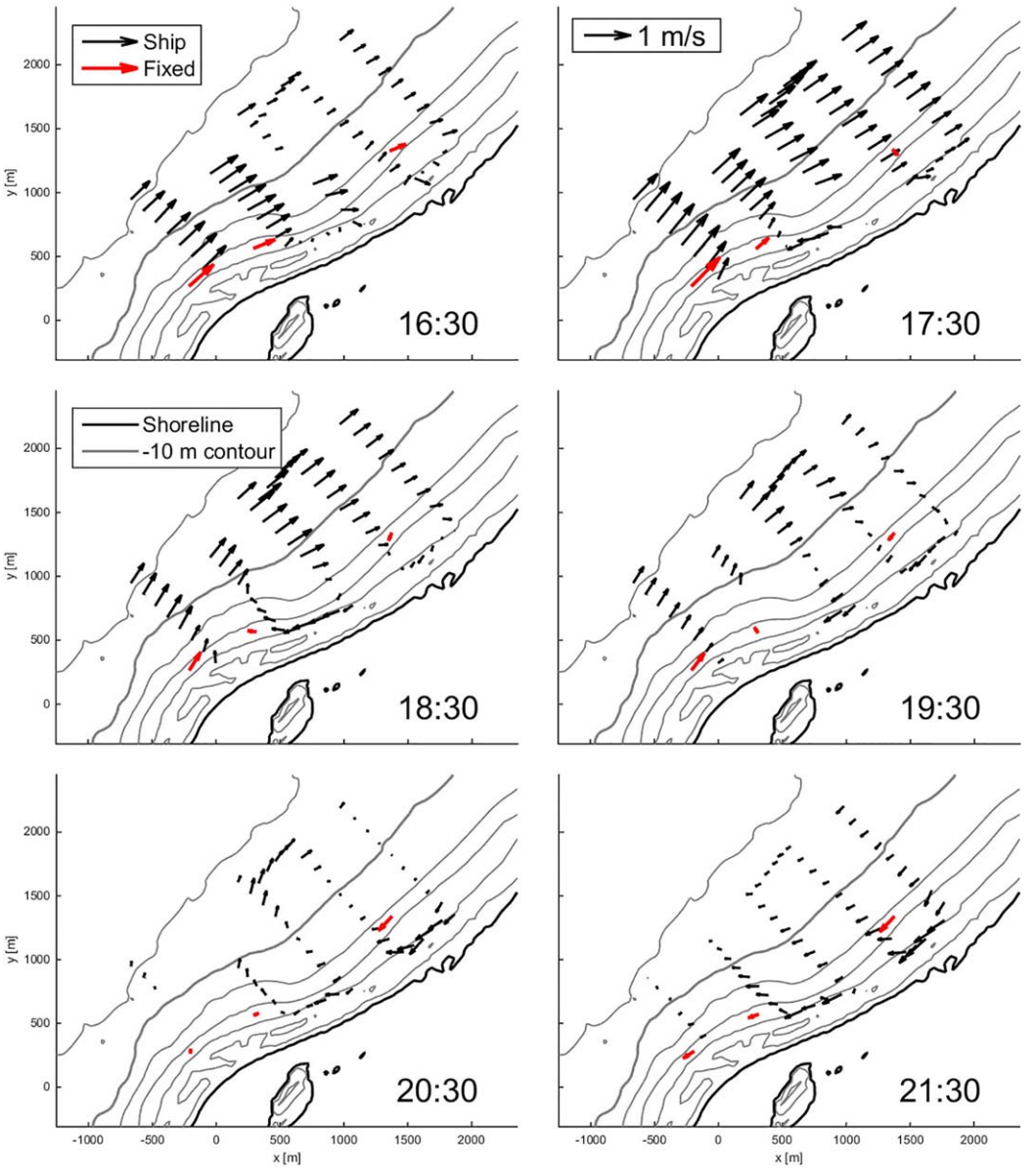

Figure 3. ADCP velocity vectors on 27 September 2014. Contours represent the bathymetry.

separating flow. Hence, it is unlikely that the observed alongshore velocity peaks are related to eddy dynamics. The effect of stratification on the tidal currents is outside the scope of this study, which focuses on tidal flow separation.

The clearest indication of flow separation in these time series is given by the negative alongshore flow velocities at stations B3 and E during the late flood phase. This signature indicates whether flow separation occurs at every tidal cycle in the 3 week deployment period. The minimum (i.e., most negative) alongshore flow velocity v_m occurring at B3, E, and F over the late flood phase is determined for every tidal cycle (Figure 5). The late flood phase is defined between 1 h before the high water peak (HW) and 2 h after HW. The results presented here showed to be rather insensitive to the exact definition of the late flood phase.

Flow reversal during the late flood phase (i.e., negative values of v_m) rarely occurs at station F, whereas this effect is present during most tidal cycles at B3 and E. At station E, a significant modulation of v_m with the peak alongshore flow velocity at A5 can be observed ($r^2=0.55$, significant to the 95% confidence level),

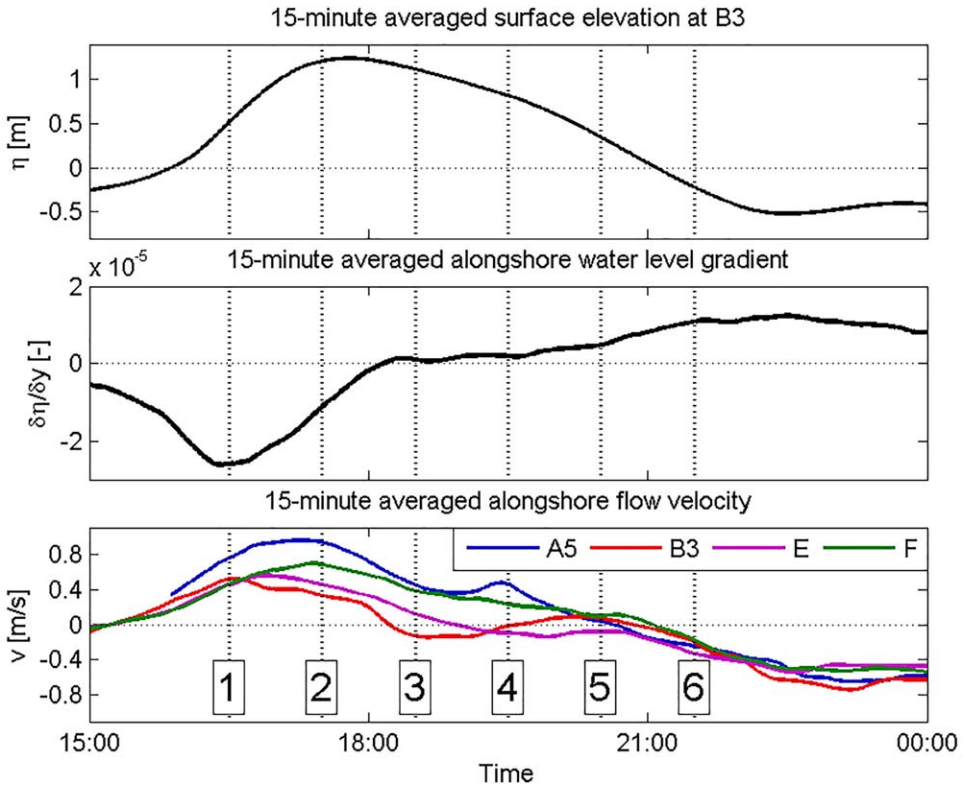

Figure 4. Observed time series of surface elevation with respect to chart datum (approximately mean sea level) at (top) station B3, (middle) alongshore water level gradient $\partial\eta/\partial y$ computed from the pressure sensors, and (bottom) alongshore flow velocity at four different stations (positive velocities in flood direction). All time series represent 15 min running averages and were observed on 27 September 2014. Six vertical lines indicate the times of the flow fields shown in Figure 3.

showing that the circulation of the eddy intensifies during spring tide. A strong correlation between v_m and the tidal range is absent at the other stations, most probably due to the fact that B3 is positioned at the edge of the tidal eddy while F is positioned outside the eddy. While winds were rather weak during the periods addressed in Figures 3 and 4, stronger winds occurred later on during the measurement period. A moderate correlation is found between the alongshore wind speed and v_m at station B3 ($r^2 = 0.44$, significant to the 95% confidence level), while this correlation is very weak or absent at the other stations. Possibly, the presence of alongshore winds leads to slight horizontal shifts in eddy position, locating B3 further inside or outside the eddy. As tidal currents are the focal point of this study, the influence of wind on tidal eddy behavior is not considered here in further detail.

4. Numerical Model Setup and Comparison to Field Data

A numerical model is employed to fill in spatial and temporal details of the field data and to study scenarios involving different nourishment geometries and tidal characteristics. The outline of the model is presented in this section, together with a comparison of computed tidal currents and the field observations.

4.1. Model Setup

The depth-averaged (2-D-horizontal) model is constructed with the modeling package Delft3D [*Lesser et al.*, 2004], which numerically integrates the shallow water equations. The parameter sensitivity study (section 5) is aimed at assessing the tidal flow around various nourishment geometries in different tidal environments at an alongshore uniform coastline. This requires a schematized model setup, without the specific characteristics of the Delfland coast (Figure 2). The nourishment geometry was superimposed on an alongshore uniform coastal bathymetry, with a cross-shore depth profile which is representative of the average profile along the Delfland coast. Prescribed water levels along the offshore boundary were interpolated from time series at both offshore corners, ensuring that a tidal phase difference builds up along the boundary. The

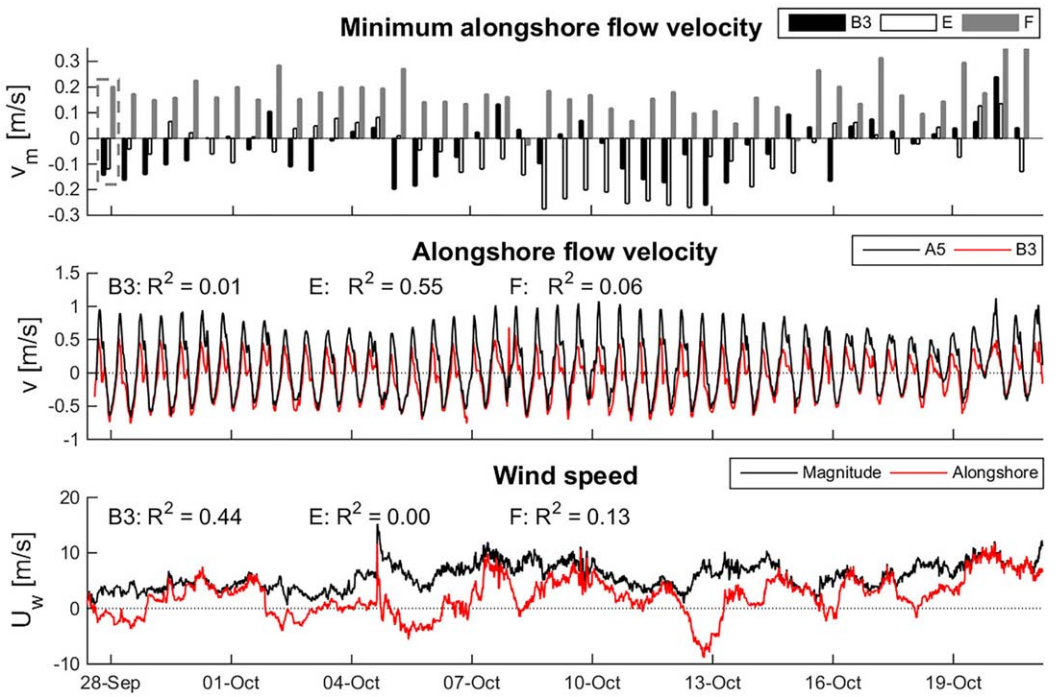

Figure 5. Long-term analysis of the fixed ADCP time series. (top) The minimum alongshore velocity parameter (v_m) is shown for stations B3, E, and F. (middle) The full time series of alongshore flow velocity at stations A5 and B3, including squared correlation coefficients between v_m and the peak tidal flow velocity at A5 during every individual tidal cycle. (bottom) Wind speed magnitude and alongshore wind speed (positive alongshore winds coming from the South-West), including squared correlation coefficients between v_m and the alongshore wind speed averaged over every individual tidal cycle. The tidal cycle containing the ship-mounted ADCP measurements is boxed in the top plot.

lateral boundaries were forced with Neumann conditions, which prescribe the alongshore water level gradient. This gradient was calculated from the difference between the water levels in both corner points divided by the alongshore domain length. Although this method does not exactly reproduce the local gradients along the cross-shore boundaries, the model is found to be rather insensitive to the Neumann boundaries. Water levels at the offshore corner points were obtained from the Continental Shelf Model and the nested Dutch Coast Model [*Sembiring et al*., 2015], which were forced with astronomic water levels at the Western European continental shelf break.

For the parameter sensitivity study, artificial time series of water levels were imposed at the offshore corner points. These time series were constructed from the M2 constituent only. The M2 phase difference between both offshore corner points, which drives the alongshore tidal currents in the model domain, was derived from the Dutch Coast Model.

Friction is specified using the White-Colebrook formulation with wall roughness height parameter $k = 0.025$ m, which has been calibrated by minimizing the root-mean-squared error between modeled and observed (fixed and ship-mounted ADCP's) currents and water levels. The model calculates spatially and temporally varying turbulent viscosities based on Horizontal Large Eddy Simulation [*Uittenbogaard and Van Vossen*, 2003] with an averaging duration of 30 min and a background viscosity of 0.01 m^2/s. All model simulations were initiated with an 11 day spin-up period, which allowed the model to reach stable conditions.

The model bathymetry applied to compare the model with field data was based on bimonthly RTK-DGPS surveys of the Sand Motor. The GPS instrumentation was mounted on a personal watercraft with a single-beam echo sounder for the subaqueous parts of the measurement domain and on an all-terrain vehicle for the dry beach [*De Schipper et al*., 2016]. These data were interpolated to the rectangular model grid, which has a variable spatial resolution depending on the size of the modeled perturbation, such that the cross-shore size of the perturbation spans at least 10 grid cells. A numerical time step of 12 s was applied. Further grid refinement and shorter time steps were tested, but the model was found to be insensitive to these

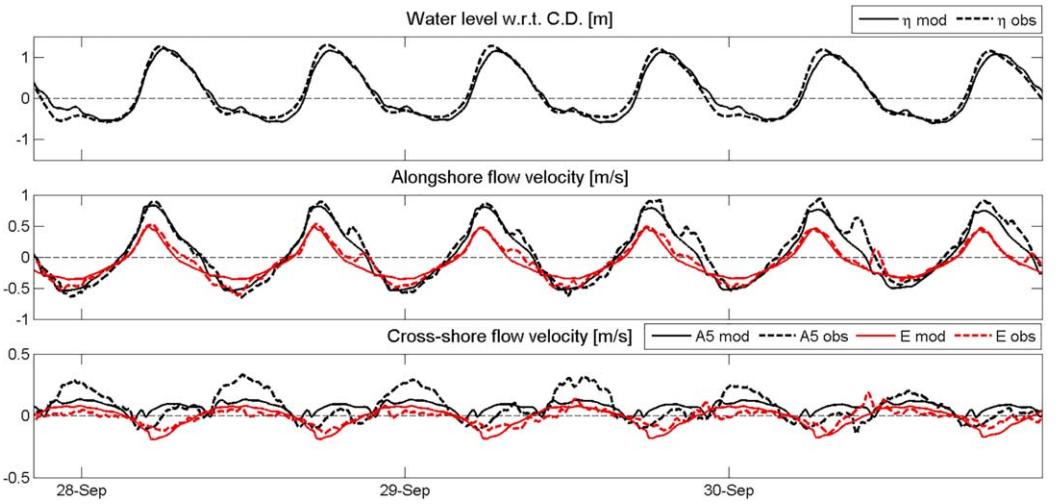

Figure 6. Comparison of model results (solid lines) to pressure sensor and ADCP field observations (dashed lines). Computed parameters are compared to (top) surface elevations from pressure sensor P_{south} as well as (middle) alongshore and (bottom) cross-shore depth-averaged flow velocities from ADCP A5 and E. Positive velocities indicate flow in flood and offshore direction, respectively.

changes. For the parameter sensitivity study, artificial nourishment designs were constructed using a cosine-shaped shoreline perturbation with a period (i.e., alongshore length scale) of $2L_a$ and an amplitude (i.e., cross-shore length scale) of $L_c/2$.

4.2. Comparison to Field Data

The numerical model was compared to the field observations presented in section 3. Comparison to the fixed ADCP velocities primarily indicates if the model is able to reproduce the basic alongshore tidal flows, although especially alongshore velocity time series at stations B3 and E also contain a clear signature of tidal flow separation and eddy formation. The ability of the model to reproduce the formation and development of tidal eddies is addressed more extensively by comparing model results to the ship-mounted ADCP data set.

First, 3 day time series from two ADCP stations and one pressure sensor are examined (Figure 6). South-easterly to south-westerly winds ranged between 3 and 6 m/s over the 3 day period shown in the figure. During the same period, the offshore wave height increased from 0.3 to 0.9 m. Modeled surface elevations largely show the same behavior as the observed surface elevations (Figure 6, top). Computed alongshore flow velocities at both stations shown in the figure compare well with the observed values in terms of amplitude, phase and tidal asymmetry (middle). The weak winds and low waves present during the 3 day analysis period have very limited impact on the observed alongshore flow, implying that the flow field is dominated by the astronomic tide.

Cross-shore velocities computed by the model show slightly larger deviations with respect to the observed flow velocities (Figure 6, bottom). Offshore velocity peaks during the ebb phase are underestimated by the model. Secondary forcing mechanisms like stratification and curvature-induced circulation, which are omitted in the schematized model, may impact the relatively weak cross-shore flows during this phase of the tide. In the time series of alongshore flow velocity, the influence of these forcing mechanisms is not visible, except for the positive peak during the late flood phase. As noted before, comparison with X-band radar imagery [*Radermacher et al.*, 2015] suggest that these peaks coincide with the arrival of the freshwater front.

Error metrics over the full measurement period (Table 2) show that at all four fixed ADCP stations, alongshore flow velocities are predicted with a root-mean-squared error between 0.05 and 0.08 m/s, giving confidence in model skill regarding alongshore tidal flow. The relative error in modeled cross-shore currents, which are 1 order of magnitude smaller than alongshore currents, is clearly larger. The difference between modeled and observed cross-shore currents is thought to be largely related to stratification and secondary

Table 2. Time Series Error Statistics

Station	RMSE (m)	Alongshore RMSE (m/s)	Cross-Shore RMSE (m/s)	Record Length (days)
A5		0.079	0.150	23.36
B3		0.080	0.131	23.40
E		0.057	0.121	34.42
F		0.046	0.107	34.52
P_{north}	0.218			33.19
P_{south}	0.218			33.21

circulations, as commonly observed in river bends and around headlands [*Geyer*, 1993]. These vertical circulations cannot be captured by the 2-D-horizontal numerical model.

The quality of the spatial flow fields calculated by the model is assessed by comparing model outcomes to the ship-mounted ADCP observations. Computed flow velocities were collected at the same spatial grid points as shown in Figure 3, taking into account the time lag between subsequent velocity profile samples along the ship's navigation tracks (Figure 7). Generally, the model is able to predict the separating tidal flow field, in terms of spatial structure as well as timing. Modeled swirling strength fields, computed as the complex part of the eigenvalues of the velocity gradient tensor [e.g., *Henriquez et al*., 2014] support interpretation of eddy development. The visual comparison of velocity vectors is quantified by direct comparisons of computed and observed velocity magnitude and direction (Figure 8), which are composed of all gridded velocity data points throughout the 13 h measurement period. Root-mean-squared errors of flow velocity magnitude are 0.05 and 0.06 m/s during the ebb and flood phase respectively. Around slack tide, the error is slightly higher (0.10 m/s). Flow velocity directions show larger deviations (Figure 8, left), although the bulk of the data points still shows good agreement between the model and the observations. Altogether, the 2DH model forced with astronomic tidal boundary conditions accurately predicts spatial and temporal evolution of the tidal flow field around the Sand Motor, including the occurrence of flow separation and eddy formation.

5. Simulated Tidal Flows Around Coastline Perturbations

A general understanding of the impact of protruding beach nourishments on the tidal flow is created based on numerical model simulations. First, a set of parameters is defined to characterize the degree of disturbance of the tidal flow field by the nourishment by quantifying the size, strength, and longevity of generated tidal eddies.

Several methods for definition and detection of eddies in an instationary flow field were considered. Often, eddy dynamics are studied from parameters that are based directly on the velocity gradient tensor (e.g., vorticity [*Long and Özkan-Haller*, 2009], swirling strength [*Henriquez et al*., 2014], and vector potentials [*Talstra*, 2011]). Reliable, automated quantification of eddy size and longevity from such parameter fields proved to be difficult. The most consistent agreement with visual eddy identification was obtained using cross-shore profiles of alongshore flow velocity v (Figure 9). The full analysis procedure makes use of 10 equally spaced transects on either side of the nourishment between the tip and the connection with the surrounding shoreline. The presence of a return flow in the shoreward part of the profile is taken as an indication of the presence of a tidal eddy. The size of the eddy L_e is defined by integrating these profiles in cross-shore direction until a zero net discharge is found. The maximum value found over 10 cross-shore profiles is assigned to L_e, which is made dimensionless through dividing by the cross-shore nourishment size L_c, resulting in dimensionless eddy scale ℓ_e. Furthermore, the strength of the eddy is characterized by the maximum swirling strength λ_{ci} found in the region delineated by the first and last cross-shore velocity profile (Figure 9) and the -1.5 and -12 m water depth contours. It has been confirmed from visual inspection that this definition leads to the maximum λ_{ci} near the eddy core if the flow separates. Swirling strength can be interpreted as the inverse rotation time scale of a vortex, which is then scaled with an inverse time scale relating to the perturbation U_p/L_c to obtain dimensionless eddy intensity Λ. As for the calculation of K_C and Re_z, U_p is defined here in an offshore grid cell, far away for the perturbation.

The evolution of ℓ_e and Λ over one tidal half-cycle in a baseline simulation (Tidal amplitude of 0.5 m, deep water tidal flow velocity amplitude of 0.35 m/s, $L_a = 1000$ m, $L_c = 300$ m) is now treated as an example (Figure 10). The tidal eddy on the downstream side of the nourishment is initiated around the peak of the main tidal flow at 0.5 h, well before the large-scale pressure gradient changes sign and turns adverse. Hence, in this simulation, tidal eddies are generated by a local adverse pressure gradient in the lee of the nourishment as a result of lateral flow expansion. ℓ_e grows at a constant rate until the large-scale pressure gradient

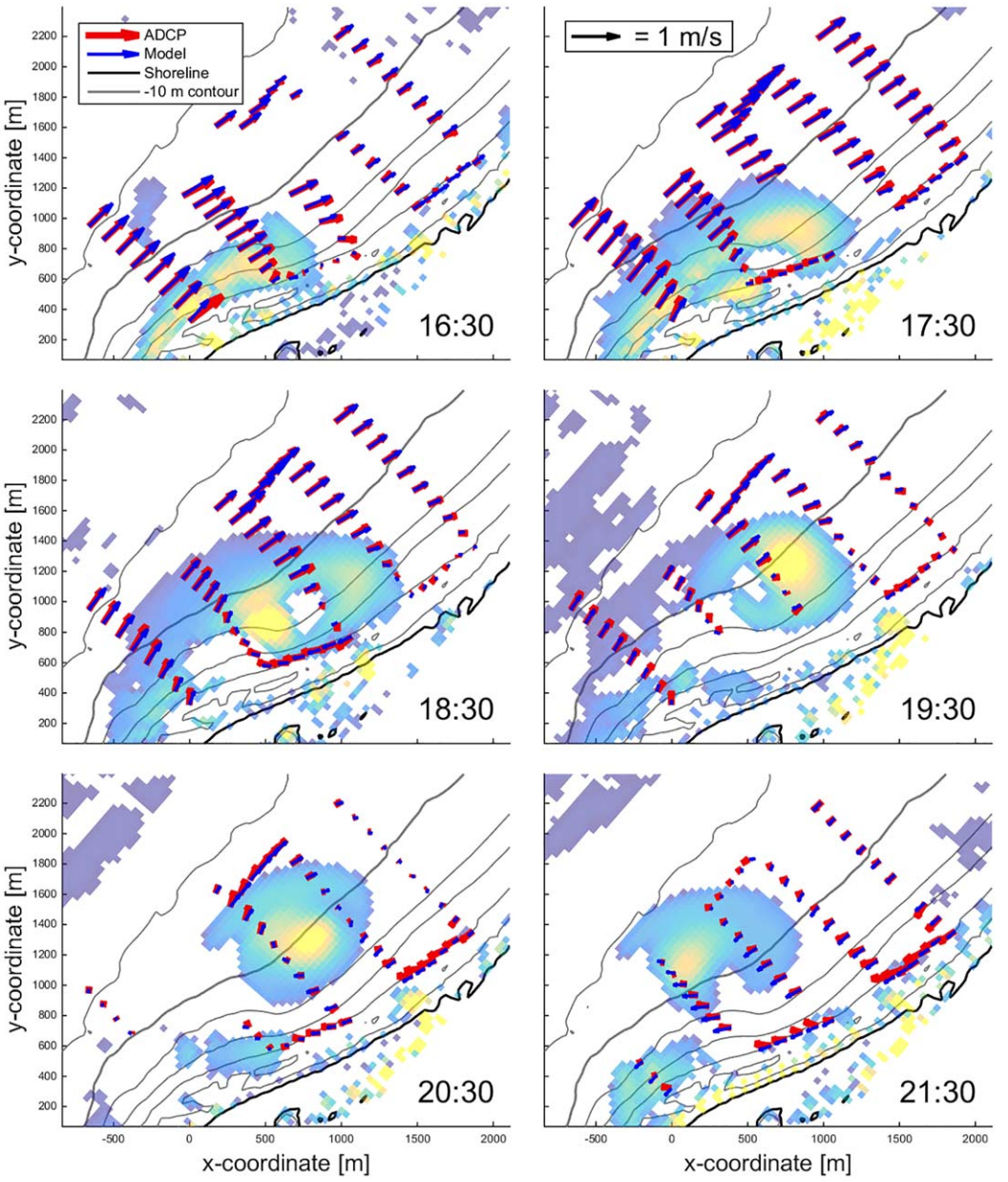

Figure 7. Comparison of model results to depth-averaged ship-mounted ADCP observations at two different moments during the flood phase. Projected local coordinates are provided along the axes. The shading represents swirling strength derived from the numerical model results to help interpretation of the flow fields. The maximum swirling strength λ_{ci}, indicated in yellow, amounts 1.0^{-3} s^{-1}.

changes sign at 3.2 h (this moment is henceforth referred to as the *pressure switch*). From the pressure switch onward, ℓ_e grows exponentially, supported by the large-scale adverse pressure gradient. Eddy intensity Λ is relatively low at the moment of eddy formation, but grows rapidly to reach its maximum value at the pressure switch. After the pressure switch, the main flow is not forced anymore and the eddy intensity is reduced, while the return flow keeps expanding and smoothly evolves into the next phase of the tidal flow.

Three parameters are now extracted from these time series of ℓ_e and Λ, such that one parameter value is obtained for every tidal half-cycle (one during flood flow and one during ebb flow). ℓ_{e0} is the downstream value of ℓ_e at the pressure switch. A nonzero value of ℓ_{e0} indicates that the initiation of the tidal eddy is caused by a locally adverse pressure gradient due to lateral flow expansion rather than a large-scale adverse pressure gradient due to the tide. The larger ℓ_{e0}, the larger the tidal flow disturbance caused by the

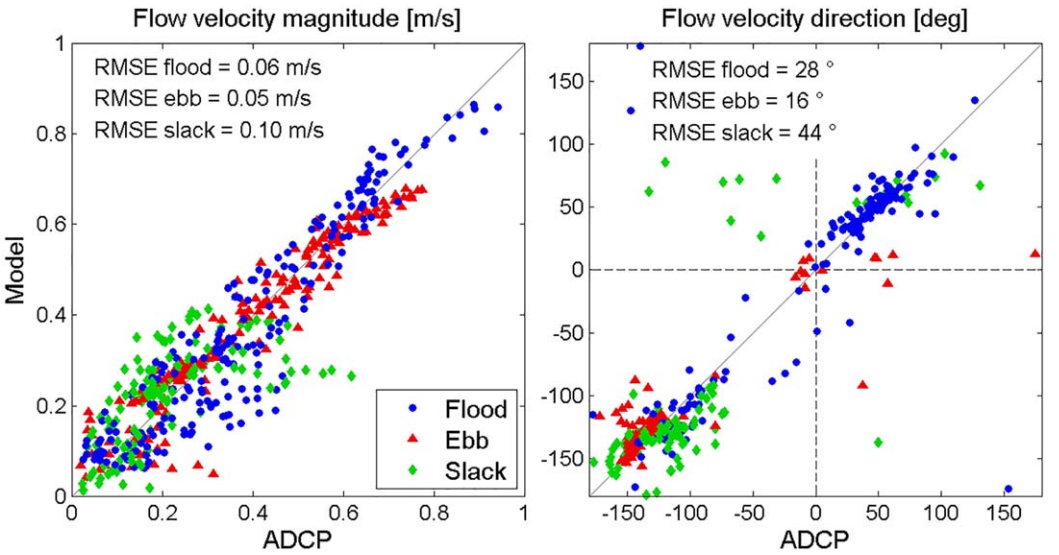

Figure 8. Direct comparison of flow velocity magnitude and direction from model results against ship-mounted ADCP observations. The different data point markers indicate different phases of the tidal flow. Root-mean-squared errors are indicated in the figure. Data points with a velocity magnitude below 0.1 m/s have been omitted from the right plot.

nourishment. Analogous considerations hold for Λ_0, the value of Λ at the pressure switch: a larger value means stronger disturbance. The third parameter is the total lifetime duration of the eddy, indicated in the top plot of Figure 10. It is expressed by T_e, and made dimensionless with the tidal period T, resulting in dimensionless eddy lifetime τ_e.

These three parameters, which describe the process of tidal flow separation for every tidal half-cycle, are now used to create a generic picture of tidal flow separation around a beach nourishment of arbitrary size and shape in an arbitrary tidal environment. A set of 29 numerical model runs with varying K_C (i.e., varying nourishment size relative to the tidal excursion, equation (1) and varying α (i.e., varying nourishment shape, equation (2) is evaluated (Figure 11). K_C is varied by changing L_a, while α is varied by changing L_c. Well-developed eddies, with a lifetime $\tau_e > 0.35$, are found for pronounced perturbations ($\alpha > 0.15$). Relative eddy size ℓ_{e0} is largest for small nourishments compared to the tidal excursion length. For $K_C > 33$ and $\alpha > 0.2$, eddy size at the pressure switch is more than twice as large as the cross-shore nourishment dimension. For very mild perturbations ($\alpha < 0.15$), no significant eddy formation takes place before the pressure switch. Eddy intensity Λ_0 is close to zero and eddy lifetime is short. Local adverse pressure gradients downstream of the nourishment tip are absent or too weak to induce flow reversal. Similarly, for very large perturbations ($K_C < 5$), no significant eddy development is found given the small eddy size and lifetime. The alongshore perturbation dimension is very large compared to the tidal excursion length. As a result, the flow field is not given enough time to spin-up during a tidal half-cycle. Local accelerations dominate advection and the flow experiences the nourishment as a smooth coastline modulation. Maximum eddy intensity is found in the upper left corner of the K_C-α plane. This implicitly shows that eddy intensity increases with increasing L_c (given that the flow separates), as the largest cross-shore

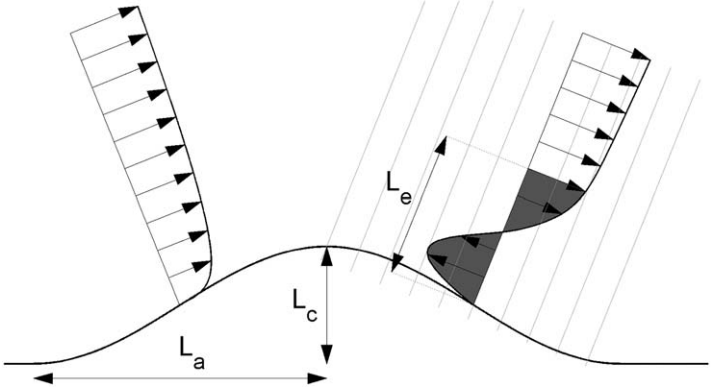

Figure 9. Definition of parameters characterizing eddy size, based on 10 downstream cross-shore transects of tidal flow velocity at the pressure switch. Velocity profiles in one upstream and one downstream transect are shown as an example.

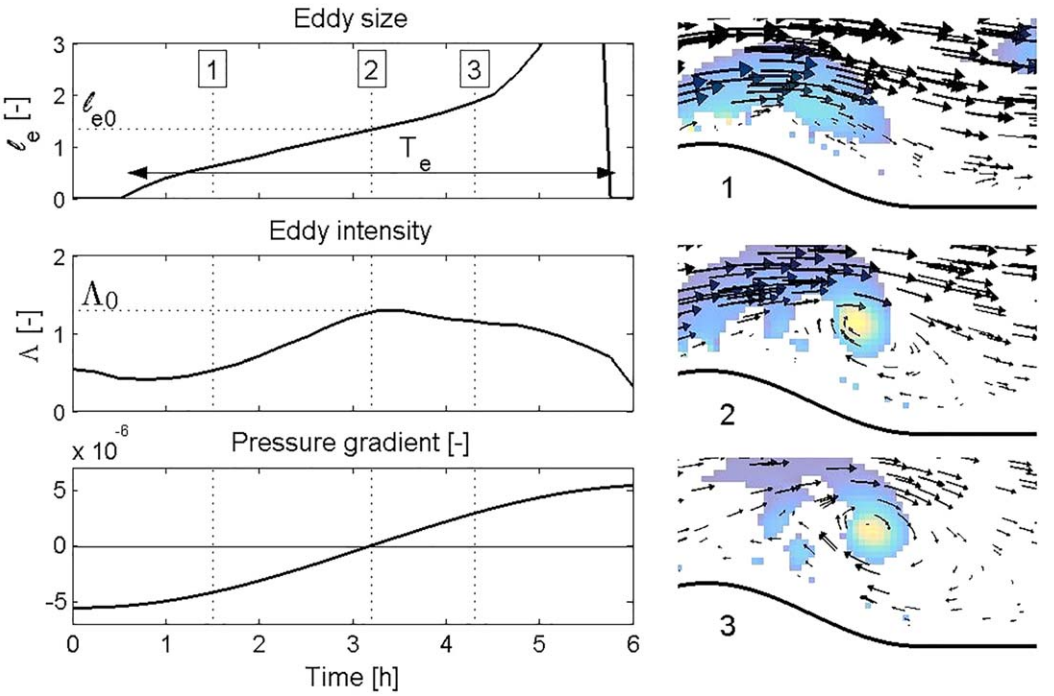

Figure 10. Time series of (top right) ℓ_e, (middle left) Λ, and (bottom left) domain-averaged alongshore pressure gradient. Vertical dotted lines indicate the times of three flow fields shown in the right plots. Line number 2 is situated at the pressure switch. A positive pressure gradient supports ebb flow (right to left), and a negative pressure gradient supports flood flow (left to right). Shading in the right plots represents computed swirling strength.

perturbation dimensions and eddy intensities are found for small K_C and large α. These perturbations with large L_c extend into deeper waters, which decreases the influence of friction and therefore allows for more intense eddies.

Visualized flow fields at the pressure switch aid interpretation of these results (Figure 12). Pronounced perturbations (large α) are found to generate circular eddies, while the eddy shape is elliptic in case of mild perturbations (small α). For relatively large perturbations (small K_C), the eddy remains close to the perturbation tip. In contrast, if the perturbation is relatively small (large K_C), the eddy core drifts farther downstream and expands into the lee zone behind the perturbation. This expansion explains the large eddy size found for large K_C.

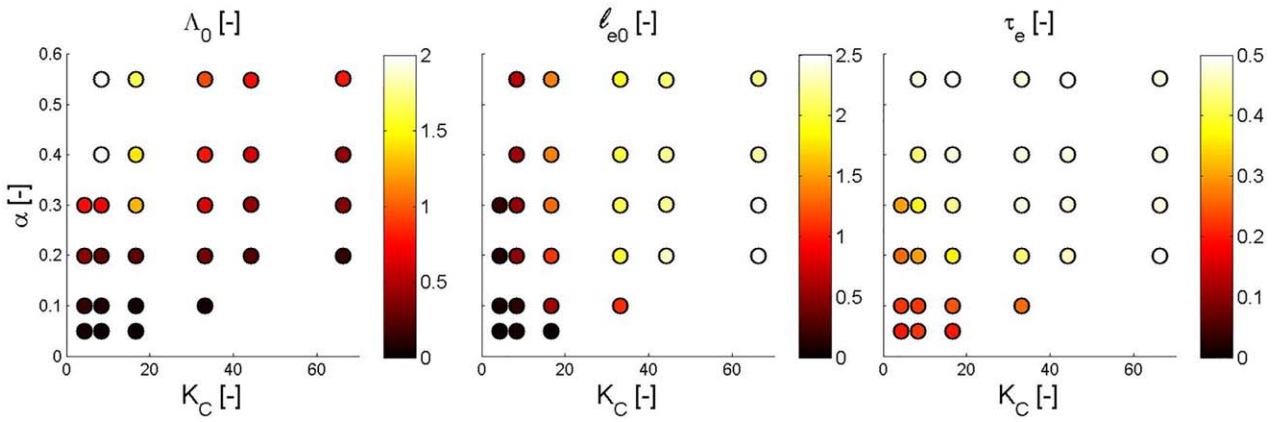

Figure 11. Various eddy characteristics as a function of K_C and α. (left) Λ_0, (middle) ℓ_{e0}, and (right) τ_e. Shaded markers show actual data points obtained from numerical simulation, a lighter color indicating stronger disturbance. These parameter values were derived from the flood half-cycle.

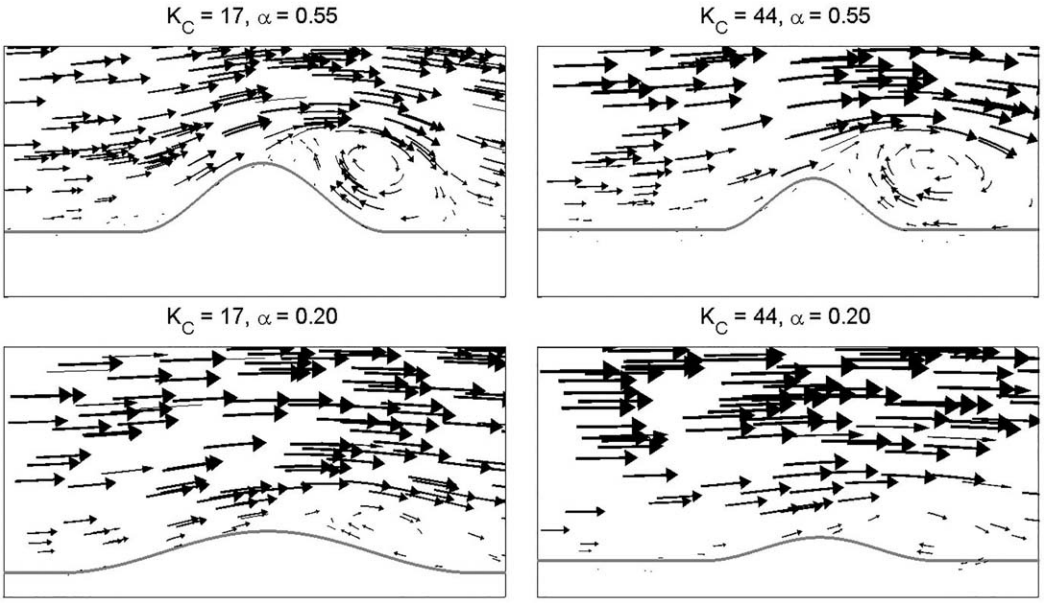

Figure 12. Comparison of the tidal flow field at the pressure switch for four runs with different K_C and α. The vector arrows are aligned with the local streamlines and provide an indication of the flow field. Arrow length and thickness increase with increasing flow velocity.

6. Discussion

The model results presented in the previous section can be schematized into several different characterizations of the tidal flow field, depending on the values of K_C and α (Figure 13). For sufficiently large or mild nourishments (low K_C or α), the coastline perturbation is not pronounced enough to induce tidal flow separation before the pressure switch. The transitional value for α is found between 0.1 and 0.2, which is similar to the empirical limit of 1/6–1/8 for separation of stationary flows [e.g., *Chandavari and Palekar*, 2014]. These results suggest that the instationary character of the flow does not affect this limit aspect ratio for flow separation. Within the parameter range where flow separation occurs before the pressure switch, several different types of eddy dynamics can be discerned. For relatively large perturbations (regions 1 and 3 in the figure), the eddy stays close to the nourishment tip and remains limited in size compared to the nourishment dimensions. For smaller perturbations (regions 2 and 4), the eddy expands toward the adjacent coastline downstream of the nourishment, allowing for a large eddy size compared to the nourishment. If the nourishment size is decreased further (region 5), the flow becomes semistationary and tidal eddies are shed off the perturbation. This regime mainly occurs outside the parameter space of the sensitivity study presented in the previous section, but is added for the sake of completeness. If the nourishment is very pronounced (regions 1 and 2), the eddy has a circular shape. For milder nourishments (regions 3 and 4), the eddy becomes more elliptic, with its cross-shore dimension significantly shorter than its alongshore dimension.

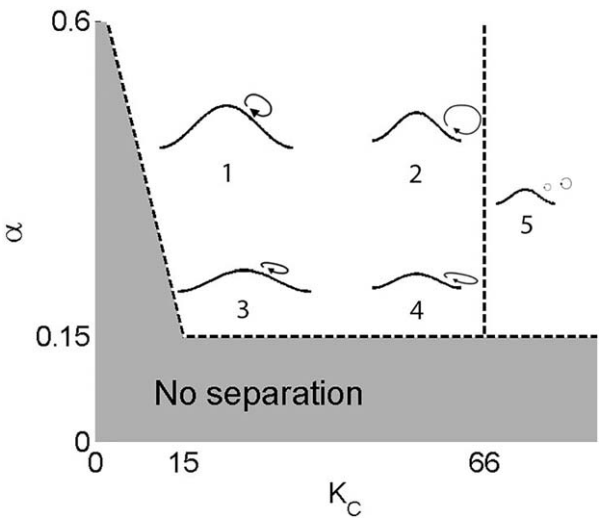

Figure 13. Generalized overview of the tidal flow disturbance by beach nourishments as a function of K_C and α. Approximate transitional values are given along the axes. Gradual transition zones exist between the regions indicated in the diagram. The vertical line at K_C = 66 indicates the extent of the modeled parameter space.

The analysis of separating tidal flow fields under varying perturbation shape and for a

wide range of K_C values elaborates upon the conceptual picture presented by *Signell and Geyer* [1991] for a pronounced headland ($\alpha = 4$). Their case with high friction and low K_C corresponds to region 1 in Figure 13. The other regions in the figure are a transitional case of their framework (region 2) or describe less pronounced aspect ratios (regions 3 and 4). Vortex shedding, as predicted by *Signell and Geyer* [1991] in model simulations with low friction, did not occur in most model simulations of the present study. Only at $K_C = 66$ the tidal eddies started to exhibit instabilities, which has been identified as a transitional case to vortex shedding at intermediate values of the shallow water Reynolds number Re_z by *Wolanski et al*. [1984]. The low-friction regime is considered less relevant for the present study, as large-scale beach nourishments are only a viable option along relatively shallow, sandy shelf coasts. The cross-shore coastal profile applied in this study, which was based on the average profile of the Delfland coast, is considered to be a typical setting for these nourishments. If the cross-shore profile is twice as steep, the nourished volume of sand (which is considered to be the governing design parameter) is confined to a smaller cross-shore extent, which limits the influence of a steeper profile on the characteristic water depth. Nevertheless, it should be noted that in case of a steeper profile, Re_z increases to O(10) and eddy instability and vortex shedding occur at somewhat lower K_C values already, which was also found from additional model simulations for these conditions (not presented here). If the tidal flow can be considered as semistationary (at high K_C), the degree of eddy instability and vortex shedding is expected to vary with Re_z as found by *Wolanski et al*. [1984] and *Tomczak* [1988].

Flow forcing due to Earth's rotation was not included in the model simulations. If the nourishment dimensions are very large, the Coriolis term has a small but noticeable influence on the flow field. An additional model simulation at $K_C = 8$ and α=0.55 with a Coriolis parameter representing conditions at 50°N causes up to 8% deviations in eddy characteristics compared to the values presented in Figure 11. If cross-shore and vertical currents are concerned, the influence of Coriolis is expected to be more important.

The field data obtained around the Sand Motor in September 2014 can now be assessed in the light of the framework in Figure 13. During the flood phase at the Sand Motor, K_C is approximately 14. The September 2014 shoreline geometry of the mega-nourishment can be approximated by a cosine function with $\alpha \sim 0.3$. According to the framework, this is a transitional case between regions 1 and 3, which matches the observations from the ship-mounted ADCP (Figure 3). A slightly elliptical eddy develops along the northern edge of the Sand Motor, quite close to the nourishment tip. At the pressure switch (around 19:00 h on 27 September 2014, Figure 4), the values of ℓ_{e0} and τ_e can be visually estimated from the ship-mounted ADCP data ($\ell_{e0} \sim 1.25$ and $\tau_e \sim 0.36$). The estimated eddy size and longevity match the values predicted from Figure 11 (ℓ_{e0}=1.2, middle, and τ_e=0.4, right). Altogether, the framework presented in this section can be used to predict or explain the tidal flow field around coastline perturbations in shallow waters. As beach nourishments tend to diffuse along the coast over time, the change of the tidal flow field with morphological evolution can be predicted.

It is expected that the presence of tidal flow separation and eddy generation significantly increases particle dispersion around protruding beach nourishments [*Signell and Geyer*, 1990]. Alongshore directed tidal particle trajectories are deformed when particles enter large-scale eddies. On short time scales (i.e., within one tidal half-cycle), this adds an important cross-shore component to the particle trajectory. On longer time scales, it leads to nonclosed tidal excursion loops and therefore to persistent dispersion of particles carried with the tidal flow. This process has implications for several aspects, ranging from morphology and ecology to water quality and recreational safety. Notably, data presented by *Huisman et al*. [2016] show a strong correlation between the presence of fine sediment in the bed and the locations of tidal eddies at the Sand Motor. Quantification of dispersion by protruding beach nourishments and its implications are an important topic for future work.

7. Conclusions

In this study, the behavior of the tidal flow field around protruding beach nourishments was examined. Based on a diverse field data set, obtained around the Sand Motor mega-nourishment at the Dutch coast, the separation of tidal flow in a real-world situation was analyzed. Subsequently, a validated numerical model was employed to determine the influence of changing perturbation dimensions on the character of the tidal flow field.

Results show that large-scale tidal eddies develop along the northern edge of the Sand Motor every flood period of the tide. Eddy development is found to be forced by a local adverse pressure gradient during the early tidal flow phase, and by a large-scale adverse tidal pressure gradient during the late flow phase. The intensity of the eddy modulates with the spring-neap cycle, with stronger eddies occurring during spring tide, when the peak tidal flow velocity is larger.

A validated numerical model shows the temporal development of predicted eddy size, strength, and lifetime, which were quantified by extracting eddy size and intensity from cross-shore flow velocity transects along the downstream side of the perturbation. These parameters enabled characterization of the tidal flow field around nourishments of varying relative nourishment size and shape. The dimensionless Keulegan-Carpenter number K_C quantified the size of the perturbation relative to the tidal excursion length, while the aspect ratio α quantified the perturbation shape. Numerical results show that tidal flow separation does not take place for relatively smooth or very large perturbations, as under these conditions the nourishment is not pronounced enough (low α) or too large compared to the tidal excursion (low K_C). For sufficiently small and pronounced perturbations (high K_C and α), flow separation occurs downstream of the nourishment tip, with generated eddies varying in strength, size, shape, and position based on the values of K_C and α. Eddies grow larger compared to the nourishment size if K_C and α increase, while the eddy intensity increases with increasing cross-shore nourishment size. The diameter of the eddies can be more than twice as large as the cross-shore nourishment dimension. For relatively small nourishments, the tidal flow becomes semi-stationary and the generated eddies are shed off the perturbation.

The field observations of eddy size and intensity obtained around the Sand Motor match the predictions made using the framework introduced in this study. These results imply that a man-made coastline perturbation can modify large-scale tidal current patterns, and generate tidal eddies at scales larger than the perturbation itself.

Acknowledgments

M.R. was supported by STW grant 12686: Nature-driven Nourishments of Coastal Systems (NatureCoast), S1: Coastal safety. M.dS. was supported by the ERC-Advanced Grant 291206—Nearshore Monitoring and Modeling (NEMO). We express our gratitude to the colleagues who helped us out in the field: Wilmar, Sierd, Bonnie, Meagan, Martijn, Bas, Marion, Duong, Nick, Caroline, Teun, Lisa, Jeroen, Emma, Pim, Marijke, Patrick, and Carolin. Harmen Talstra is thanked for his advice and assistance on the issue of eddy definition and detection. Rijkswaterstaat is gratefully acknowledged for the use of their instrumentation. We thank two anonymous reviewers for their valuable comments, which have significantly improved this paper. All data presented in this study are available upon request (m.radermacher@tudelft.nl).

References

Black, K. P., and S. L. Gay (1987), Eddy formation in unsteady flows, *J. Geophys. Res.*, *92*(C9), 9514–9522.

Chandavari, V., and S. Palekar (2014), Diffuser angle control to avoid flow separation, *Int. J. Tech. Res. Appl.*, *2*(5), 16–21.

Dankert, H., J. Horstmann, and W. Rosenthal (2003), Ocean wind fields retrieved from radar-image sequences, *J. Geophys. Res.*, *108*(C11), 3352, doi:10.1029/2003JC002056.

De Boer, G. J., J. D. Pietrzak, and J. C. Winterwerp (2006), On the vertical structure of the rhine region of freshwater influence, *Ocean Dyn.*, *56*, 198–216.

De Schipper, M. A., S. De Vries, G. Ruessink, R. C. De Zeeuw, J. Rutten, C. Van Gelder-maas, and M. J. F. Stive (2016), Initial spreading of a mega feeder nourishment: Observations of the sand engine pilot project, *Coastal Eng.*, *111*, 23–38.

De Vriend, H. J., M. Van Koningsveld, S. G. J. Aarninkhof, M. B. De Vries, and M. J. Baptist (2015), Sustainable hydraulic engineering through building with nature, *J. Hydro-environ. Res.*, *9*(2), 159–171.

Ferentinos, G., and M. Collins (1980), Effects of shoreline irregularities on a rectilinear tidal current and their significance in sediment processes, *J. Sediment. Petrol.*, *50*(4), 1081–1094.

Geyer, W. R. (1993), Three-dimensional tidal flow around headlands, *J. Geophys. Res.*, *98*(C1), 955–966.

Geyer, W. R., and R. P. Signell (1990), Measurements of tidal flow around a headland with a shipboard acoustic doppler current profiler, *J. Geophys. Res.*, *95*(C3), 3198–3197.

Haller, M. C., D. Honegger, and P. A. Catalan (2014), Rip current observations via marine radar, *J. Waterway Port Coastal Ocean Eng.*, *140*(2), 115–124.

Hamm, L., M. Capobianco, H. H. Dette, A. Lechuga, R. Spanhoff, and M. J. F. Stive (2002), A summary of European experience with shore nourishment, *Coastal Eng.*, *47*, 237–264.

Hench, J. L., and R. A. Luettich Jr. (2003), Transient tidal circulation and momentum balances at a shallow inlet, *J. Phys. Oceanogr.*, *33*, 913–932.

Henriquez, M., A. J. H. M. Reniers, G. Ruessink, and M. J. F. Stive (2014), PIV measurements of the bottom boundary layer under nonlinear surface waves, *Coastal Eng.*, *94*, 33–46.

Huisman, B. J. A., M. A. De Schipper, and B. G. Ruessink (2016), Sediment sorting at the Sand Motor at storm and annual time scales, *Mar. Geol.*, *381*, 209–226.

Lesser, G. R., J. A. Roelvink, J. A. T. M. Van Kester, and G. S. Stelling (2004), Development and validation of a three-dimensional morphological model, *Coastal Eng.*, *51*, 883–915.

Long, J. W., and H. T. Özkan-Haller (2009), Low-frequency characteristics of wave group-forced vortices, *J. Geophys. Res.*, *114*, C08004.

Nowell, A. R. M., and P. A. Jumars (1984), Flow environments of aquatic benthos, *Annu. Rev. Ecol. Syst.*, *15*, 303–328.

Pattiaratchi, C., A. James, and M. Collins (1986), Island wakes and headland eddies: A comparison between remotely sensed data and laboratory experiments, *J. Geophys. Res.*, *92*(C1), 783–794.

Pingree, R. D. (1978), The formation of the shambles and other banks by tidal stirring of the seas, *J. Mar. Biol. Assoc. U. K.*, *58*, 211–226.

Radermacher, M., W. Zeelenberg, M. A. De Schipper, and A. J. H. M. Reniers (2015), Field observations of tidal flow separation at a mega-scale beach nourishment, paper presented at Coastal Sediments, San Diego, Calif.

Ralph, M. E. (1986), Oscillatory flow in wavy-walled tubes, *J. Fluid Mech.*, *168*, 515–540.

Sembiring, L., M. Van Ormondt, A. Van Dongeren, and D. Roelvink (2015), A validation of an operational wave and surge prediction system for the Dutch coast, *Nat. Hazards Earth Syst. Sci.*, *15*, 1231–1242.

Signell, R. P., and W. R. Geyer (1990), Numerical simulation of tidal dispersion around a coastal headland, in *Residual Currents and Long-term Transport, Coastal and Estuarine Studies*, vol. 38, edited by R. T. Cheng, Springer, New York, N. Y.
Signell, R. P., and W. R. Geyer (1991), Transient eddy formation around headlands, *J. Geophys. Res.*, *96*(C2), 2561–2575.
Simpson, R. L. (1989), Turbulent boundary-layer separation, *Annu. Rev. Fluid Mech.*, *21*, 205–234.
Sobey, I. J. (1983), The occurrence of separation in oscillatory flow, *J. Fluid Mech.*, *134*, 247–257.
Souza, A. J., and J. H. Simpson (1997), Controls on stratification in the rhine rofi system, *J. Mar. Syst.*, *12*, 311–323.
Stive, M. J. F., M. A. De Schipper, A. P. Luijendijk, S. G. J. Aarninkhof, C. Van Gelder-maas, J. S. M. Van Thiel de Vries, S. De Vries, M. Henriquez, S. Marx, and R. Ranasinghe (2013), A new alternative to saving our beaches from sea-level rise: The Sand Engine, *J. Coastal Res.*, *29*(5), 1001–1008, doi:10.2112/JCOASTRES-D-13-00070.1.
Talstra, H. (2011), Large-scale turbulence structures in shallow separating flows, PhD thesis, Delft Univ. of Technol., Delft, Netherlands.
Tomczak, M. (1988), Island wakes in deep and shallow water, *J. Geophys. Res.*, *93*(C5), 5153–5154.
Uittenbogaard, R. E., and B. Van Vossen (2003), Subgrid-scale model for quasi-2d turbulence in shallow water, in *International Symposium on Shallow Flows*, edited by W. S. J. Uijttewaal and G. H. Jirka, Taylor & Francis, Delft, Netherlands.
Van den Hoek, R. E., M. Brugnach, J. P. M. Mulder, and A. Y. Hoekstra (2014), Analysing the cascades of uncertainty in flood defence projects: How "not knowing enough" is related to "knowing differently", *Global Environ. Change*, *24*, 373–388.
Wijnberg, K. M. (2002), Environmental controls on decadal morphologic behaviour of the Holland coast, *Mar. Geol.*, *189*, 227–247.
Wolanski, E., J. Imberger, and M. L. Heron (1984), Island wakes in shallow coastal waters, *J. Geophys. Res.*, *89*(C6), 10,553–10,569.